Seismic Azimuthal Anisotropy Beneath the Alaska Subduction Zone

Chuanming Liu[1,2] ![ORCID], Anne F. Sheehan[3] ![ORCID], and Michael H. Ritzwoller[2]

[1]Institute for Geophysics & Department of Earth and Planetary Sciences, Jackson School of Geosciences, The University of Texas at Austin, Austin, TX, USA, [2]Department of Physics, University of Colorado Boulder, Boulder, CO, USA, [3]Cooperative Institute for Research in Environmental Sciences and Department of Geological Sciences, University of Colorado Boulder, Boulder, CO, USA

Abstract We estimate depth-dependent azimuthal anisotropy and shear wave velocity structure beneath the Alaska subduction zone by the inversion of a new Rayleigh wave dispersion dataset from 8 to 85 s period. We present a layered azimuthal anisotropy model from the forearc region offshore to the subduction zone onshore. In the forearc crust, we find a trench-parallel pattern in the Semidi and Kodiak segments, while a trench-oblique pattern is observed in the Shumagins segment. These fast directions agree well with the orientations of local faults. Within the subducted slab, a dichotomous pattern of anisotropy fast axes is observed along the trench, which is consistent with the orientation of fossil anisotropy generated at the mid-ocean ridges of the Pacific-Vancouver and Kula-Pacific plates that is preserved during subduction. Beneath the subducted slab, a trench-parallel pattern is observed near the trench, which may indicate the direction of mantle flow.

Plain Language Summary The azimuthal anisotropy of seismic waves refers to the directional dependence of the seismic wave propagation speed. We present a comprehensive azimuthal anisotropy model of the Alaska subduction zone to a depth of 200 km, revealing anisotropy caused by local faults and fractures, fossil anisotropy inherited from the oceanic plate within the subducted slab, and sub-slab mantle flow. The along-strike variation of crustal anisotropy indicates variations in the stress regime in the forearc region. The along-strike variation of anisotropy within the subducted slab identifies different origins of the subducted slab. Our model contributes to the understanding of the anisotropic structure and the sources of anisotropy in subduction zones.

1. Introduction

The Alaska subduction system is one of the most tectonically active convergent margins worldwide. Ranging from the Denali Fault in the north to the Aleutian trench in the south, volcanoes are prevalent and megathrust earthquakes ($Mw \geq 8$) have occurred in this region (Figure 1a). Although the subducting lithosphere in the Alaska subduction zone exhibits a relatively consistent convergence rate, plate age (ca. 50 ∼ 55 Ma, Müller et al., 2008), and uniform slab dip (Lallemand et al., 2005), the observed seismicity shows strong along-strike variation (e.g., Wei et al., 2021). Understanding these along trench differences is one of the motivations for the Alaska Amphibious Community Seismic Experiment (AACSE) (Abers, 2018; Barcheck et al., 2020).

Numerous studies have considered the on-continent seismic structure of the Alaska subduction zone, utilizing the USArray Transportable Array (TA) and the other regional networks (Busby & Aderhold, 2020). Both isotropic and anisotropic structures onshore have been resolved using surface waves (e.g., Feng et al., 2020; Feng & Ritzwoller, 2019; Liu et al., 2022a; Liu & Ritzwoller, 2024; Y. Wang & Tape, 2014; Yang & Gao, 2020), body waves (e.g., Eberhart-Phillips et al., 2006; Gou et al., 2019), receiver functions (e.g., Haws et al., 2023; Miller & Moresi, 2018; Schulte-Pelkum et al., 2020), joint inversion of surface waves and receiver functions (e.g., Berg et al., 2020; Gama et al., 2021; Martin-Short et al., 2018), joint inversion of surface waves and body waves (e.g., Jiang et al., 2018; Nayak et al., 2020), local shear wave splitting (Karlowska et al., 2021; Lynner et al., 2024; Richards et al., 2021), SKS shear wave splitting (e.g., Birkey & Lynner, 2024; McPherson et al., 2020; Venereau et al., 2019), and Pn tomography (He & Lü, 2021).

In contrast, the offshore forearc region have been much less investigated. Seismic reflection/refraction studies have provided high-resolution velocity profiles (e.g., Li et al., 2015; Shillington et al., 2015) that extend into the lower crust. With the deployment of the AACSE ocean-bottom seismometer (OBS) stations, the isotropic seismic

Writing – review & editing:
Chuanming Liu, Anne F. Sheehan, Michael H. Ritzwoller

structure has been resolved using surface waves (e.g., Feng, 2021; Li et al., 2024) and body waves (e.g., Gou et al., 2022; F. Wang et al., 2024). However, information about anisotropy has only been provided by shear wave splitting at a subset of the AACSE stations (Lynner, 2021). A better understanding of the anisotropic structure of the Alaska subduction zone is needed to illuminate potential along-strike structural variations in anisotropic fabric and, consequently, perhaps volatile content (Lynner, 2021) and deformation (Liu & Ritzwoller, 2024).

In this study, we construct an azimuthally anisotropic shear wave velocity model of the crust and uppermost mantle beneath the Alaska subduction zone. We use a new Rayleigh wave dispersion database across Alaska and the subduction zone (Liu et al., 2022a). The database is built using two- and three-station ambient noise interferometry and earthquake data. The application of three-station interferometry bridges asynchronous seismic stations and improves the ray path coverage (Zhang et al., 2020), which is particularly important for the OBS stations (Liu et al., 2022a). Our purpose is to investigate the azimuthal anisotropic structure of the Alaska subduction zone and infer the fast-axis direction variations along the strike of the trench.

Our depth-dependent azimuthally anisotropic model is constructed with the working assumption of a hexagonally symmetric medium with a horizontal symmetry axis: a horizontal transverse isotropic (HTI) medium. An HTI medium is consistent with anisotropy produced by fractures, faults, and olivine dominating the oceanic mantle (e.g., Crampin, 1987; Hess, 1964). The resolved anisotropy is "apparent", however, because we assume the orientation of the symmetry axis rather than estimating it (Xie et al., 2017). A complete investigation would include the estimation of the dip angle of the symmetry axis, as was done by Liu and Ritzwoller (2024) for the onshore region. This is beyond the scope of the present work, however, because it requires Love wave observations. We argue here that the working assumption reveals valuable information about past and present deformation in the crust and mantle of the Alaska subduction system.

2. Rayleigh Wave Phase Speed Azimuthal Anisotropy Tomography

We apply Rayleigh wave phase speed dispersion measurements (8–85 s) from the surface wave dispersion database constructed by Liu et al. (2022a). Here, we summarize the data processing and tomography performed in that study. Liu et al. (2022a) present a detailed discussion of the entire data processing procedure, including a quantification of the uncertainties of the phase speed measurements.
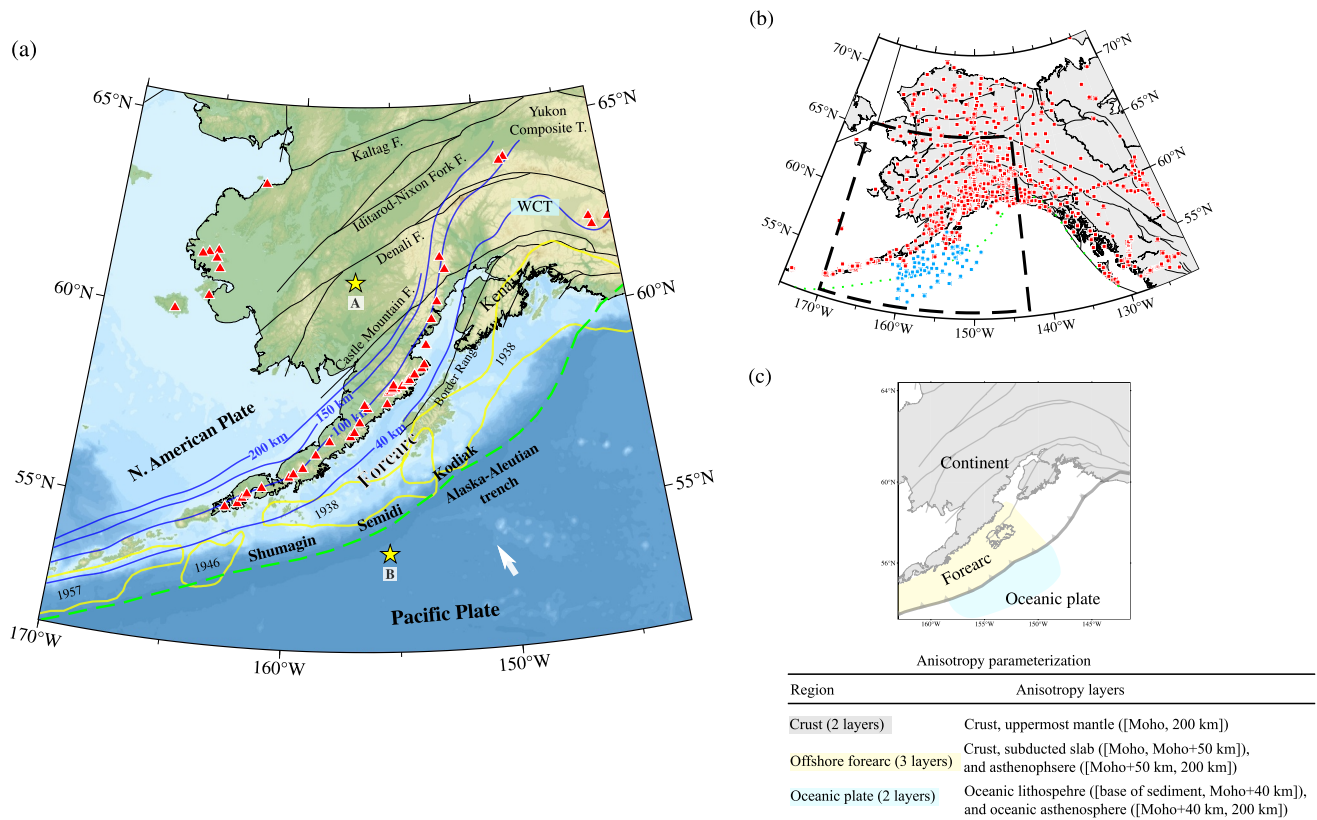
The surface wave dispersion dataset is constructed using two- and three-station ambient noise interferometry and earthquake data based on seismic stations deployed from January 2000 to October 2020 both onshore and offshore across Alaska. There are a total of 979 seismic stations used, including 75 ocean bottom seismometers (OBS) from AACSE. The earthquake data encompasses 3,395 teleseismic events with a $Ms > 5.5$ that occurred during the period of station deployment. The distribution of seismic stations is shown in Figure 1b. Station spacing is variable but averages about 80 km.

Rayleigh wave phase speed measurements are obtained by applying automatic frequency-time analysis (FTAN, e.g., Levshin & Ritzwoller, 2001) to two- and three-station ambient noise data and earthquake data. Both earthquake data and estimated Green's functions from interferometry are subjected to a signal-to-noise ratio (SNR) threshold of 10. Three-station interferometry enhances SNR and bridges asynchronous receiver-station pairs, approximately doubling the total number of measurements.

The local Rayleigh wave isotropic phase speed and azimuthal anisotropy are directly estimated on a 0.2° (longitude) by 0.1° (latitude) grid (~11 km) using eikonal tomography (Lin et al., 2009) for ambient noise data (8–50 s) and Helmholtz tomography (Lin & Ritzwoller, 2011a) for earthquake data (28–85 s). Considering the azimuthal dependence of Rayleigh wave phase speed in a weakly anisotropic medium, the local phase speed for azimuth ψ is parameterized as (e.g., Smith & Dahlen, 1973),

$$c(\psi) = c_{iso}(1 + \delta c_{AA}(\psi)) = c_{iso}\left(1 + \frac{A_1}{2}\cos(\psi - \psi_1) + \frac{A_2}{2}\cos 2(\psi - \psi_2)\right) \tag{1}$$

where c_{iso} is the isotropic phase speed, δc_{AA} is the azimuthal anisotropy perturbation, ψ_1 and ψ_2 are the fast axes for the 1ψ and 2ψ components of anisotropy, and A_1 and A_2 are the peak-to-peak relative amplitudes for the 1ψ and 2ψ anisotropy, respectively. The 1ψ anisotropy is strongest at long periods and is not caused by intrinsic anisotropy, but is an isotropic phenomenon that may be caused by several effects, including Rayleigh wave back-

Figure 1. Tectonic settings, seismic station distribution in Alaska, and regionalization of seismic anisotropy. (a) Reference map for southwest Alaska. The black curves are major faults (ending with "F."). The four blue contours represent the upper surface of the subducted slab at different depths (40, 100, 150, and 200 km) based on the Slab2.0 model (Hayes et al., 2018). The red triangles denote volcanoes. A few tectonic terranes, mountain ranges, and faults (Colpron et al., 2007) are labeled. WCT: Wrangellia composite terrane. Yellow stars are the example points used in Figure S1 in Supporting Information S1. The white arrow indicates the direction of motion of the Pacific Plate relative to North America. The yellow polygons show the rupture zones of historical megathrust earthquakes (Tape & Lomax, 2022). The green dashed line shows the plate boundary between the Pacific and North American Plates. (b) Seismic stations: red squares for onshore stations and blue squares for OBS instruments from the AACSE. The dashed box is the study region of this paper. (c) Regionalization of azimuthal anisotropy model. Azimuthal anisotropy is defined by two layers on the Alaskan continent (the gray-shadowed region) and the incoming oceanic plate (the blue-shadowed region), and by three layers in the interpreted forearc region (the yellow-shadowed region), which is the focus of this paper.

scattering (Lin & Ritzwoller, 2011b). Liu et al. (2022a) find that below 50 s period $A_1 \ll A_2$. We estimate 1ψ and 2ψ anisotropy simultaneously at periods above 50 s to remove 1ψ bias. Helmholtz tomography is also used for earthquake data for periods at and above 28 s to reduce the influence of finite frequency effects.

In our study, we directly use the composite Rayleigh wave isotropic phase speed and 2ψ azimuthal anisotropy (fast axis, ψ_2, and amplitude, A_2) and corresponding uncertainties from Liu et al. (2022a). Examples of azimuthally binned Rayleigh wave phase speed measurements at Points A and B (identified in Figure 1) are shown in Figure S1 in Supporting Information S1. Examples of the composite Rayleigh wave isotropic phase speed and azimuthal anisotropy at different periods are shown in Figure S2 in Supporting Information S1.

3. Model Parameterization and Inversion

We apply a two-step inversion procedure to resolve the depth-dependence of both the shear-wave speed (Vsv) and azimuthal anisotropy (e.g., Lin et al., 2011). In this context, we define Vsv as $V_{SV} = \sqrt{\frac{L}{\rho}}$, where L is one of the elastic Love moduli (A, C, L, N and F), and ρ is density. The subscript 'V' in Vsv indicates the transverse direction in the context of 'transverse isotropy'. In the first step, we use the isotropic Rayleigh wave phase speed and uncertainty to construct an isotropic Vsv model on a 0.4°(longitude) by 0.2° (latitude) grid using Bayesian Monte Carlo inversion (e.g., Feng & Ritzwoller, 2019; Shen & Ritzwoller, 2016). The model represents Vsv as linearly increasing in the sedimentary layer, with four B-splines in the crystalline crust and five B-splines in the uppermost

mantle to a depth of 200 km. The water depth is fixed in wet regions to the value from the ETOPO1 bathymetry model (Amante & Eakins, 2009). The starting or reference model for Monte Carlo sampling is a composite of the *Vsv* model onshore of Feng and Ritzwoller (2019) and the *Vsv* model offshore of Feng (2021). The prior distribution for each parameter is determined by the reference model with prior constraints on each parameter. The details of prior constraints and perturbation ranges are described in Table S1 in Supporting Information S1. To establish a transversely isotropic reference model, defined in terms of A, C, L, N and F, we set $N = L$, $A = C$, $C = \kappa^2 L$, $\kappa = V_P/V_S$ ratio, and $F = A - 2L$.

In the second step, after we have estimated the *Vsv* reference model, we introduce more simply parameterized azimuthal anisotropy perturbations to fit the azimuthal anisotropy of Rayleigh wave phase speed at each location. The azimuthal anisotropy in the continental and oceanic plate regions is defined by one crustal layer and one mantle layer (Figure 1c). However, in the offshore forearc subduction zone, it is defined by *one* crustal layer and *two* mantle layers: one for the subducted slab and one for the asthenosphere. This is based on the variation of the fast direction pattern in the Rayleigh wave phase velocity azimuthal anisotropy from short to long periods in this region (Figure S2 in Supporting Information S1). The details of the layered anisotropy parameterization are described in Figure 1c. In a weak anisotropic medium, the azimuthal anisotropic perturbation to the Rayleigh wave phase speed (Montagner & Nataf, 1986) can be interpreted as follows:

$$\delta c_{AA}(T, \psi) = \int_0^\infty \left\{ \left(G_c \frac{\partial c_R}{\partial L} + B_c \frac{\partial c_R}{\partial A} + H_c \frac{\partial c_R}{\partial F} \right) \cos 2\psi + \left(G_s \frac{\partial c_R}{\partial L} + B_s \frac{\partial c_R}{\partial A} + H_s \frac{\partial c_R}{\partial F} \right) \sin 2\psi \right\} dz \quad (2)$$

where δc_{AA} is defined in Equation 1, T is period, the anisotropic shear moduli $G_{c,s}$, $B_{c,s}$, *and* $H_{c,s}$ represent the 2ψ azimuthal variations for three (L, A, and F) of the five Love moduli, and $\frac{\partial c_R}{\partial L}$, $\frac{\partial c_R}{\partial A}$, and $\frac{\partial c_R}{\partial F}$ are the sensitivity kernels for L, A, and F, respectively. We ignore the term $H_{c,s}$ due to its small impact on Rayleigh wave phase speed (e.g., Montagner & Nataf, 1986). We also impose the relationship, $\frac{B_{c,s}}{A} = \frac{G_{c,s}}{L}$, following Lin et al. (2011), Liu et al. (2019), and Feng et al. (2020), based on studies of mica- and amphibole-rich crustal rocks (Barruol & Kern, 1996) as well as olivine-dominated mantle rocks (Montagner & Nataf, 1986). Therefore, Equation 2 can be written approximately as

$$\delta c_R(T, \psi) = \int_0^\infty \left\{ \left(\frac{\partial c_R}{\partial L} + \frac{A}{L} \frac{\partial c_R}{\partial A} \right) G_c \cos 2\psi + \left(\frac{\partial c_R}{\partial L} + \frac{A}{L} \frac{\partial c_R}{\partial A} \right) G_s \sin 2\psi \right\} dz \quad (3)$$

In Equation 3, we only estimate the anisotropic shear moduli $G_{c,s}$ in the second step of the inversion. We use the Rayleigh wave phase speed azimuth anisotropy (ψ_2, A_2) measurements to invert for the $G_{c,s}$ as constant values in two layers for the continental region (crust and mantle) and oceanic plate (lithosphere and asthenosphere) and three layers for the forearc offshore region (crust, subducted slab, and asthenosphere) by Bayesian Monte Carlo inversion. The depth-dependent fast azimuth, ϕ_{SV}, and anisotropy amplitude, A_{SV}, are determined from G_s and G_c as follows:
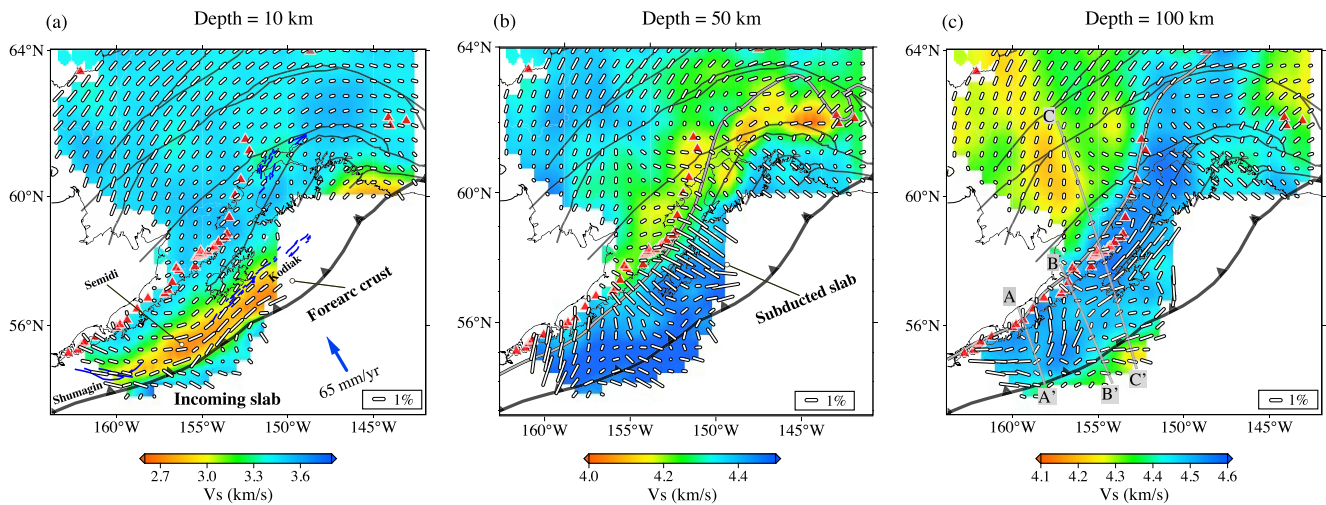
$$\phi_{SV} = \frac{1}{2} \tan^{-1} \left(\frac{G_s}{G_c} \right) \quad (4)$$

and

$$A_{SV} = \frac{1}{2} \sqrt{ \left(\frac{G_s}{L} \right)^2 + \left(\frac{G_c}{L} \right)^2 } \quad (5)$$

We estimate the uncertainties of ϕ_{SV} and A_{SV} using an error transfer formula (e.g., Liu et al., 2019; Yuan & Beghein, 2018).

Figure 2. Azimuthal anisotropy near the Alaskan subduction zone. Azimuthal anisotropy maps at depths of (a) 10, (b) 50, and (c) 100 km. The white bars indicate the fast axis directions of anisotropy at each depth, where the lengths are proportional to the amplitude. The background maps show isotropic shear wave speed (*Vsv*) at the corresponding depth. Black lines represent large-scale faults. In (a), blue lines represent local faults (Horowitz et al., 1989; Koehler, 2013); a blue arrow indicates the direction of motion of the Pacific Plate. The upper surface of the subducting slab from Slab 2.0 is marked with a gray line in (b)–(c). (c) Similar to (a), but showing the profiles AA', BB', and CC' used in Figure 3.
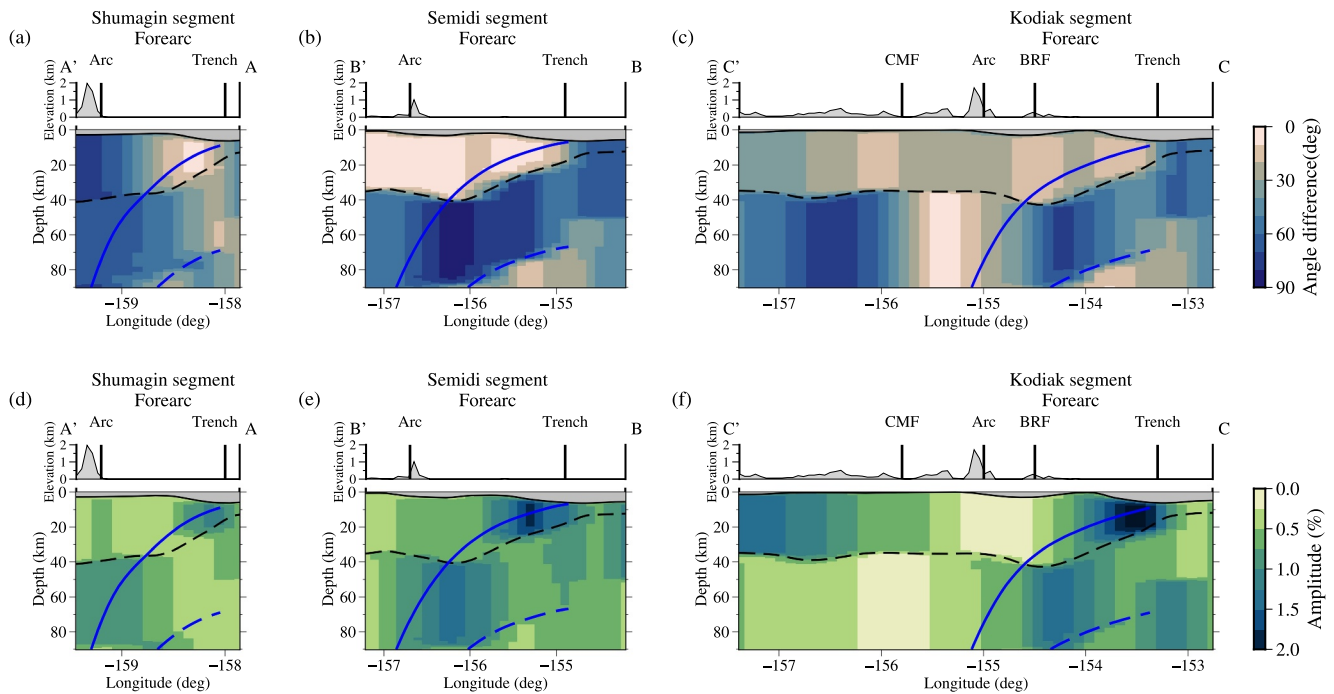
4. Results

We estimate the depth-dependent posterior distributions from Bayesian Monte Carlo inversion for each model parameter discussed in Section 3. We discuss the mean and standard deviation of the posterior distribution for isotropic *Vsv* and azimuthal anisotropy fast direction and amplitude (ϕ_{SV} and A_{SV}) as functions of depth. An example of the prior distributions and posterior distributions for isotropic *Vsv* at a single location is shown in Figure S3 in Supporting Information S1. The isotropic *Vsv* structure, defined as the mean of the posterior distribution at each grid location, is shown in Figure S4 in Supporting Information S1 and details are described in Text S1 in Supporting Information S1. Uncertainty estimates for isotropic *Vsv* are presented in Figure S5 in Supporting Information S1.

Figure 2 shows the depth-dependent azimuthal anisotropy (ϕ_{SV} and A_{SV}) at three depths, determined from the mean of the posterior distribution at 10, 50, and 100 km. Figure 3 shows the angle difference between the fast axis direction and the trench orientation and the amplitude of anisotropy along the three profiles AA', BB', and CC' (Figure 2c) across the three forearc segments: Shumagins, Semidi, and Kodiak, respectively. Uncertainty maps of azimuthal anisotropy for both fast azimuth and amplitude are shown in Figure S6 in Supporting Information S1.

At a depth of 10 km (Figure 2a), the azimuthal anisotropy reflects the features of the continental crust onshore and the forearc crust above the subducted slab, and the uppermost oceanic mantle of the Pacific Plate offshore. For the continental crust onshore, the amplitude (A_{SV}) is relatively small (Figure 2a), and the fast directions align sub-parallel to the local major faults, as reported by Feng et al. (2020) and Liu and Ritzwoller (2024). In the offshore forearc region, trench sub-parallel fast axis directions are observed with strong amplitudes in the Semidi and Kodiak segments, while fast axes are trench-oblique in the Shumagins segment (Figures 2a and 3a-c). Seaward of the trench on the oceanic plate, where the spatial extent of the model is small, the uppermost oceanic mantle shows fast directions that are nearly perpendicular to the trench (Figures 2a and 3a-c) and subparallel to the plate motion direction.

At a depth of 50 km (Figure 2b), north of the slab surface contour in the continental uppermost mantle, a curved pattern of azimuthal anisotropy is observed continentward of the subducted slab. However, north of 62°N, fast axes remains nearly the same as the directions observed in the crust (Figure 2a). Oceanward of the slab surface at 50 km depth within the subducted slab, the azimuthal anisotropy is very strong (Figures 3d–3f) and presents fast axis orientations that are trench-sub-perpendicular and trench-oblique (Figures 2b and 3a-c). However, in the region near and south of the trench, the flat-lying oceanic mantle exhibits a trench sub-parallel pattern (Figure 2b).

Figure 3. Azimuthal anisotropy profiles across the Alaska subduction zone. (a–c) The angle difference between the fast axis direction and the trench orientation along profiles AA', BB', and CC' identified in Figure 2c. (d–f) The amplitude of anisotropy along the same profiles. CMF: the Castle Mountain fault, BRF: the Border Ranges fault.

At a depth of 100 km (Figure 2c), south of and near the volcanic arc, the azimuthal anisotropy still displays a trench-perpendicular pattern (Figures 2c and 3a-c). However, near the trench, the azimuthal anisotropy shows a trench-subparallel pattern. The continental azimuthal anisotropy north of the slab surface contour remains the same as the pattern at a depth of 50 km, due to the two-layer parameterization of azimuthal anisotropy onshore.
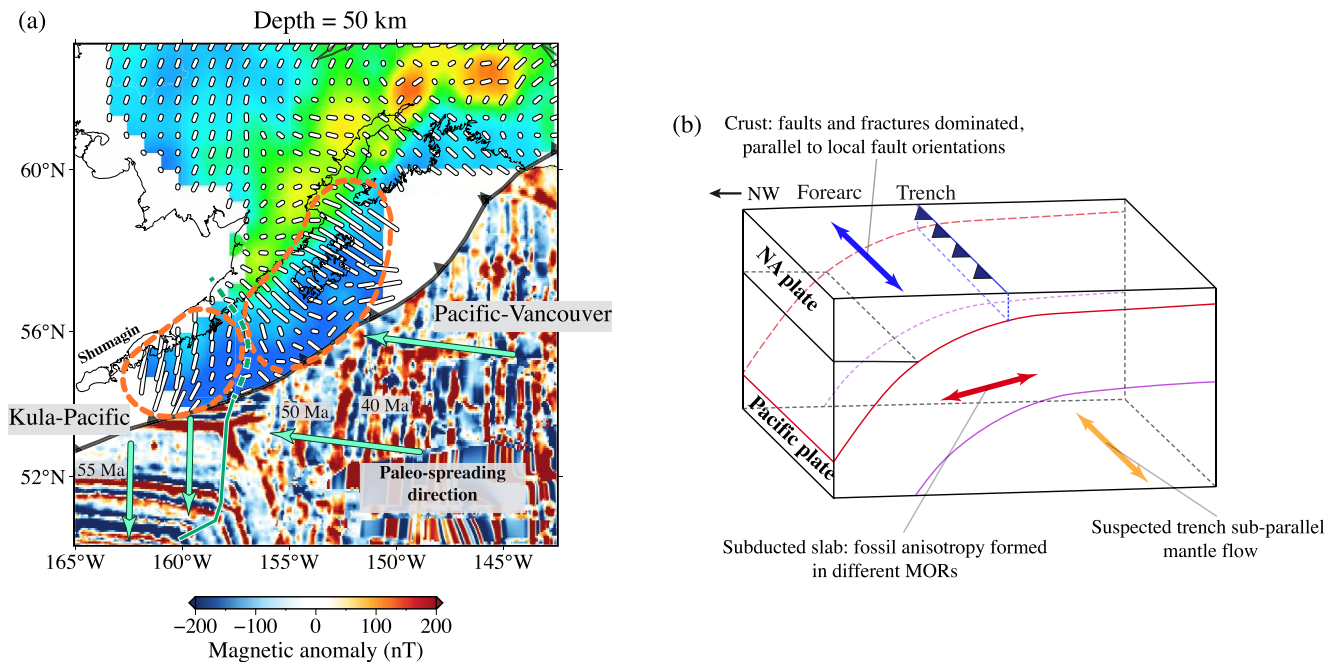
The average uncertainties for the anisotropy fast directions are approximately 8°, 12°, and 13° at depths of 20, 50, and 100 km (Figures S6a-6c in Supporting Information S1), respectively. The average uncertainty for amplitude is less than 0.2% (Figures S6d-6e in Supporting Information S1) at these depths, while the offshore region has larger uncertainty due to the more limited azimuthal coverage compared with the onshore region.

5. Discussion

5.1. Interpretation of Azimuthal Anisotropy Patterns

Above the subducted slab, in the forearc region north of the Aleutian trench, our model resolves trench-subparallel fast directions in the Semidi and Kodiak segments of the Alaskan convergent margin (Figures 2a and 3b-c). This orientation is consistent with the findings of Pn tomography (He & Lü, 2021), which is sensitive to the bottom of the crust and the top of the uppermost mantle. This trench sub-parallel pattern in the forearc crust above the subducted slab is probably caused by faults, cracks, and fractures beneath the forearc, in the accretionary wedge, and at the top of the slab. The orientations of nearby large-scale strike-slip faults, including the Border Ranges fault and the Contact fault, are also trench-parallel. Similar trench-parallel patterns in the forearc above the subducted slab have been observed in other subduction zones. For example, trench-parallel fast directions in the Tohoku forearc were reported by Z. Wang et al. (2022) from P-wave anisotropy, which they explained resulted from aligned hydrated faults on the slab's upper surface. In addition, large-scale trench-parallel fast directions in the overlying crust above the subducted Pacific slab in the forearc region of the Japan trench are resolved by Uchida et al. (2020) using local shear wave splitting.

An exception to the trench parallel pattern above the slab is the trench-oblique pattern in the Shumagins segment (Figures 2a and 3a). However, the trench-oblique fast directions still align with local normal fault orientations (Horowitz et al., 1989). The different fast direction patterns in the forearc crust indicate along-strike variations of

Figure 4. Azimuthal anisotropy and interpretation near the Alaska subduction zone. (a) Azimuthal anisotropy map at depth of 50 km (as in Figure 2b) with the magnetic anomaly map from EMAG2v3 (Meyer et al., 2017). The white bars indicate the fast axis directions of anisotropy. The cyan arrows indicate the paleo-spreading directions. The orange polygons, separated by the dashed green line, denote fossil anisotropy of subducted oceanic plates originally formed at the Kula-Pacific (western polygon) and the Pacific-Vancouver (eastern polygon) MORs. The green solid line is the oceanic plate boundary based on magnetic anomaly. The green dashed line is the suspected boundary based on the azimuthal anisotropy. (b) Interpretation of the azimuthal anisotropy pattern in the Aleutian subduction zone. The fast direction of azimuthal anisotropy within the crust above the slab is marked by the blue arrow, where the anisotropy fast directions are dominated by local faults and fractures. The fast direction within the subducted slab is marked by red arrow, where the fast directions reflect fossil anisotropy generated at different MORs and are affected by the bending of subduction. The nearly trench-parallel orange arrow below the slab is hypothesized to represent the mantle flow direction. NA = North America.

orientations of local faults and fractures, suggesting that trench-parallel strike-slip faults only dominate the Semidi and Kodiak segments. Furthermore, this indicates that transpressional deformation related to the flat-subduction of the buoyant Yakutat microplate extends to the crust of the Semidi and Kodiak segments but terminates near the boundary between the Semidi and Shumagins segments.

Seaward of the Aleutian trench (Figure 2a) in the oceanic plate we observe trench perpendicular-to-oblique fast directions in the incoming oceanic lithosphere. This observation reflects the fossil anisotropy within the oceanic Pacific plate, generated by the development of crystallographic preferred orientation (CPO) near mid-oceanic ridges (e.g., Francis, 1969).

Within the subducted slab and revealed by the high Versus isotropic anomaly strip (Figures 2b and 4a), we resolve a clear dichotomy in fast direction pattern with a boundary marked by a green-dashed line in Figure 4a. East of the boundary, in Semidi and Kodiak, the fast directions are mainly trench-sub-perpendicular; while west of the boundary, in the Shumagins, the fast directions mainly show NS orientations. These fast directions are roughly consistent with the azimuthal anisotropy in the corresponding incoming oceanic plate of each region (Figure 3a). We believe this dichotomous anisotropic pattern is controlled by the varied fossil fabrics formed at different mid-ocean ridges (MOR), a topic we discuss further in Section 5.2. Within the slab, in the region near and south of the trench, we also identify some trench-subparallel fast directions, likely caused by the influence of the trench-parallel intraslab faults (e.g., Z. Wang et al., 2022).

In the onshore forearc region, we have a single mantle layer of anisotropy. The resolved arc-perpendicular pattern (Figures 2b and 2c) in this area may result from the influence of intraslab fossil anisotropy and toroidal mantle flows. Local shear-wave splitting with short-period bandpass and small depth range (Richards et al., 2021), and SKS shear-wave splitting (e.g., McPherson et al., 2020) also reflect a similar arc-normal pattern in this region, albeit with different depth sensitivity.

Near the bottom and below the slab, we see nearly trench-parallel orientations near the trench (Figure 2c). This trench-parallel pattern may be caused by trench-parallel mantle flow (e.g., Faccenda & Capitanio, 2012; Lynner, 2021).

The azimuthal anisotropy pattern in the onshore mantle (Figure 2b) primarily reflects arc-parallel fast directions in the backarc region and an arc-normal pattern in south-central Alaska. Combined with the arc-parallel pattern in the offshore forearc region, our azimuthal anisotropy near the bottom of and below the slab generally reflects similar mantle flow regimes as revealed by SKS shear-wave splitting results (McPherson et al., 2020).

The estimated amplitude of anisotropy may be underestimated due to the assumption of a horizontal (non-tilted) symmetry axis (e.g., Xie et al., 2017). In Figures 3a–3c, the subducted slab is dipping from 0° to 40° (Figure S7 in Supporting Information S1), with an average dip angle of about 20°. Thus, the amplitude of anisotropy in the slab is probably underestimated by less than 10%, on average, which is within the estimated uncertainty.

5.2. Fossil Azimuthal Anisotropy Within the Subducted Slab

For the Pacific oceanic plate, one major cause of the observed pattern of azimuthal anisotropy is the alignment of intrinsically anisotropic olivine due to relative plate motion (i.e., paleo-spreading direction) when it was formed at the mid-ocean ridge (MOR) (e.g., Becker et al., 2014). We estimate paleo-spreading directions by computing the gradient of seafloor ages (Seton et al., 2020) with results shown as cyan arrows in Figure 4a. The boundary of fast directions (green line in Figure 4a) also demarcates the incoming oceanic plates near the Aleutian trench that were formed at different MORs. East of the boundary the oceanic plate was generated at the Pacific-Vancouver MOR; west of the boundary it was generated at the Kula-Pacific MOR.

The paleo-spreading directions from the Kula-Pacific MOR are roughly north-south, which is consistent with the azimuthal anisotropy pattern within the subducted slab beneath the Shumagins (Figure 4a). In contrast, the paleo-spreading directions from the Pacific-Vancouver MOR near the trench are predominantly east-west, while fast directions show a slightly northward deviation, which may be attributed to bending during subduction (e.g., X. Wang et al., 2022).

The dichotomy of the azimuthal anisotropy pattern within the subducted slab is inherited from the different MORs and is preserved during subduction. There have been few reports of azimuthal anisotropy within the slab in other subduction zones due to the limited distribution of OBS. X. Wang et al. (2022) reported the fast velocity direction normal to the fossil seafloor isochrons in the Sumatra subduction zone, which is mainly trench-parallel. Therefore, the seismic anisotropy fast directions within the subducted slab correspond more closely to the paleo-spreading directions rather than trench orientations.

The along-strike variations in the fossil anisotropy also present a spatial correlation with the slip deficit distribution in the forearc region (Figure S8 in Supporting Information S1, S. Li & Freymueller, 2018; F. Wang et al., 2024). The boundary of azimuthal anisotropy within the subducted slab aligns with the boundary separating the strongly locked region and the weakly locked region, indicating the impact of the different physical properties of the subducted oceanic plate that originated at different MORs.

5.3. Comparison With SKS Splitting

We compare the directional information from SKS splitting with our mantle model in order to test our model and also provide information about the depth of source of the SKS splitting. To perform the comparison, we assemble an SKS splitting dataset by combining results from McPherson et al. (2020) and Lynner (2021). The details about the construction of the SKS dataset are in Text S2 in Supporting Information S1. Because of the limited measurements in the incoming oceanic plate, we focus the comparison with our model in the uppermost mantle for the continent (Figure S9c in Supporting Information S1), the subducted slab (Figure S9d in Supporting Information S1) and the asthenosphere below the slab (Figures S9b and e in Supporting Information S1) for the offshore forearc region (yellow-shadowed region in Figure 1c).

For the continental region (Figure S9a in Supporting Information S1), the majority of the SKS fast directions align with those of our mantle model, such that 55% of the SKS splitting observations differ by less than 30° from our model with a mean difference of 32° (Figure S9c in Supporting Information S1).

For the offshore forearc region, SKS splitting fast directions show a better alignment with our model in the asthenosphere layer than within the subducted slab (Figures S9d and e in Supporting Information S1), indicating that the major source of SKS splitting lies in the deeper mantle below the slab for the offshore forearc region. There are a few stations with large angle differences near the trench in Figure S9b in Supporting Information S1 when compared to our asthenosphere layer model. However, these splitting fast directions are closer to the fast directions within the slab in our model, indicating the influence of fossil anisotropy within the slab in the area near the trench.

Onshore, the multi-layer modeling of SKS shear-wave splitting study near the Aleutians (Birkey & Lynner, 2024) also indicates multi-layered anisotropy. However, using traditional path-integral SKS shear-wave splitting analysis, it is difficult to infer multi-layered anisotropy in complex tectonic environments, such as subduction zones. If there is multi-layered anisotropy in the subduction zone, a joint inversion based on complementary datasets, such as surface waves (for top ∼150 km), receiver functions (for upper plate), local-S (for upper plate and mantle wedge) and SKS (for subslab mantle) splits, may produce better constraints on the anisotropic structure.

6. Conclusion

We present a new depth-dependent azimuthal anisotropy model of the crust and uppermost mantle beneath the Alaska subduction zone, based on a new Rayleigh wave dispersion database (Liu et al., 2022a). Our model provides detailed information about the along-strike variations in azimuthal fast directions in the crust, the subducted slab, and the uppermost mantle. As summarized by a cartoon in Figure 4b, our model highlights the vertical variations of the fast-axis in the forearc region. In the forearc crust, our model reveals a trench-parallel pattern in the Semidi and Kodiak segments, while displaying a trench-oblique pattern in the Shumagins segment. Both patterns may be caused by local faults and fractures. Within the subducted slab, we observe an along-trench fast direction dichotomy with a trench-perpendicular pattern in the Semidi and Kodiak segments and a north-south pattern in the Shumagins segment. The link of this dichotomy with nearby paleo-spreading directions indicates the presence of fossil anisotropy inherited from the Pacific-Vancouver MOR and the Kula-Pacific MOR. Additionally, in the forearc asthenosphere beneath the slab, a trench-parallel pattern is evident, potentially indicating the horizontal mantle flow directions.

Data Availability Statement

The surface wave dispersion dataset can be found at Liu et al. (2022b). The azimuthal anisotropy model presented herein are available at Liu et al. (2024). The model's authoritative version will also be available at the EarthScope Earth Model Collaboration repository. The magnetic anomaly data is from EMAG2v3 (Meyer et al., 2017). The GMT code used to create the figures is available at www.soest.hawaii.edu/gmt.

References

Abers, G. (2018). Aace: Alaska amphibious com-munity seismic experiment: International fed-eration of digital seismograph networks, https://doi.org/10.7914/SN/XO_2018

Amante, C., & Eakins, B. W. (2009). ETOPO1 global relief model converted to PanMap layer format. NOAA-National Geophysical Data Center. [Dataset]. https://doi.org/10.1594/PANGAEA.769615. *PANGAEA*

Barcheck, G., Abers, G. A., Adams, A. N., Bécel, A., Collins, J., Gaherty, J. B., et al. (2020). The Alaska amphibious community seismic experiment. *Seismological Research Letters*, *91*(6), 3054–3063. https://doi.org/10.1785/0220200189

Barruol, G., & Kern, H. (1996). Seismic anisotropy and shear-wave splitting in lower-crustal and upper-mantle rocks from the Ivrea zone: Experimental and calculated data. *Physics of the Earth and Planetary Interiors*, *95*(3–4), 175–194. https://doi.org/10.1016/0031-9201(95)03124-3

Becker, T. W., Conrad, C. P., Schaeffer, A. J., & Lebedev, S. (2014). Origin of azimuthal seismic anisotropy in oceanic plates and mantle. *Earth and Planetary Science Letters*, *401*, 236–250. https://doi.org/10.1016/j.epsl.2014.06.014

Berg, E. M., Lin, F., Allam, A., Schulte-Pelkum, V., Ward, K. M., & Shen, W. (2020). Shear velocity model of Alaska via joint inversion of Rayleigh wave ellipticity, phase velocities, and receiver functions across the Alaska transportable Array. *Journal of Geophysical Research: Solid Earth*, *125*(2). https://doi.org/10.1029/2019jb018582

Birkey, A., & Lynner, C. (2024). Multilayer anisotropy along the Alaska-Aleutians subduction zone. *Geophysical Journal International*, *237*(3), ggae137–1779. https://doi.org/10.1093/gji/ggae137

Busby, R. W., & Aderhold, K. (2020). The Alaska transportable Array: As built. *Seismological Research Letters*, *91*(6), 3017–3027. https://doi.org/10.1785/0220200154

Colpron, M., Nelson, J. L., & Murphy, D. C. (2007). Northern Cordilleran terranes and their interactions through time. *Geological Society of America Today*, *17*(4), 4. https://doi.org/10.1130/gsat01704-5a.1

Crampin, S. (1987). Geological and industrial implications of extensive-dilatancy anisotropy. *Nature*, *328*(6130), 491–496. https://doi.org/10.1038/328491a0

Eberhart-Phillips, D., Christensen, D. H., Brocher, T. M., Hansen, R., Ruppert, N. A., Haeussler, P. J., & Abers, G. A. (2006). Imaging the transition from Aleutian subduction to Yakutat collision in central Alaska, with local earthquakes and active source data. *Journal of Geophysical Research: Solid Earth (1978–2012)*, *111*(B11). n/a-n/a. https://doi.org/10.1029/2005jb004240

Faccenda, M., & Capitanio, F. A. (2012). Development of mantle seismic anisotropy during subduction-induced 3-D flow. *Geophysical Research Letters*, *39*(11), n/a-n/a. https://doi.org/10.1029/2012gl051988

Feng, L. (2021). Amphibious shear wave structure beneath the Alaska-aleutian subduction zone from ambient noise tomography. *Geochemistry, Geophysics, Geosystems*, *22*(5). https://doi.org/10.1029/2020gc009438

Feng, L., Liu, C., & Ritzwoller, M. H. (2020). Azimuthal anisotropy of the crust and uppermost mantle beneath Alaska. *Journal of Geophysical Research: Solid Earth*, *125*(12). https://doi.org/10.1029/2020jb020076

Feng, L., & Ritzwoller, M. H. (2019). A 3-D shear velocity model of the crust and uppermost mantle beneath Alaska including apparent radial anisotropy. *Journal of Geophysical Research: Solid Earth*, *124*(10), 10468–10497. https://doi.org/10.1029/2019jb018122

Francis, T. (1969). Generation of seismic anisotropy in the upper mantle along the mid-oceanic ridges. *Nature*, *221*(5176), 162–165. https://doi.org/10.1038/221162b0

Gama, I., Fischer, K. M., Eilon, Z., Krueger, H. E., Dalton, C. A., & Flesch, L. M. (2021). Shear-wave velocity structure beneath Alaska from a Bayesian joint inversion of Sp receiver functions and Rayleigh wave phase velocities. *Earth and Planetary Science Letters*, *560*, 116785. https://doi.org/10.1016/j.epsl.2021.116785

Gou, T., Xia, S., Huang, Z., & Zhao, D. (2022). Structural heterogeneity of the Alaska-aleutian forearc: Implications for interplate coupling and seismogenic behaviors. *Journal of Geophysical Research: Solid Earth*, *127*(11). https://doi.org/10.1029/2022jb024621

Gou, T., Zhao, D., Huang, Z., & Wang, L. (2019). Aseismic deep slab and mantle flow beneath Alaska: Insight from anisotropic tomography. *Journal of Geophysical Research: Solid Earth*, *124*(2), 1700–1724. https://doi.org/10.1029/2018jb016639

Haws, A. A., Long, M. D., & Luo, Y. (2023). Anisotropic structure of the normally-dipping and flat slab segments of the Alaska subduction zone: Insights from receiver function analysis. *Tectonophysics*, *868*, 230112. https://doi.org/10.1016/j.tecto.2023.230112

Hayes, G. P., Moore, G. L., Portner, D. E., Hearne, M., Flamme, H., Furtney, M., & Smoczyk, G. M. (2018). Slab2, a comprehensive subduction zone geometry model. *Science*, *362*(6410), 58–61. https://doi.org/10.1126/science.aat4723

He, Y., & Lü, Y. (2021). Anisotropic Pn tomography of Alaska and adjacent regions. *Journal of Geophysical Research: Solid Earth*, *126*(11). https://doi.org/10.1029/2021jb022220

Hess, H. (1964). Seismic anisotropy of the uppermost mantle under oceans. *Nature*, *203*(4945), 629–631. https://doi.org/10.1038/203629a0

Horowitz, W. L., Steffy, D. A., Hoose, P. J., & Turner, R. F. (1989). Geologic report for the shuamagin planning area, western gulf of Alaska. United states department of the interior, minerals management service.

Jiang, C., Schmandt, B., Ward, K. M., Lin, F., & Worthington, L. L. (2018). Upper mantle seismic structure of Alaska from Rayleigh and S wave tomography. *Geophysical Research Letters*, *45*(19), 10350–10359. https://doi.org/10.1029/2018gl079406

Karlowska, E., Bastow, I. D., Rondenay, S., Martin-Short, R., & Allen, R. M. (2021). The development of seismic anisotropy below south-central Alaska: Evidence from local earthquake shear wave splitting. *Geophysical Journal International*, *225*(1), 548–554. https://doi.org/10.1093/gji/ggaa603

Koehler, R. D. (2013). Quaternary faults and folds (QFF) (Vol. *3*). [Dataset]. https://doi.org/10.14509/24956. *Alaska Division of Geological & Geophysical Surveys Digital Data Series*.

Lallemand, S., Heuret, A., & Boutelier, D. (2005). On the relationships between slab dip, back-arc stress, upper plate absolute motion, and crustal nature in subduction zones. *Geochemistry, Geophysics, Geosystems*, *6*(9). n/a-n/a. https://doi.org/10.1029/2005gc000917

Levshin, A. L., & Ritzwoller, M. H. (2001). Automated detection, extraction, and measurement of regional surface waves. *Monitoring the Comprehensive Nuclear-Test-Ban Treaty: Surface Waves*, 1531–1545. https://doi.org/10.1007/978-3-0348-8264-4_11

Li, J., Shillington, D. J., Bécel, A., Nedimović, M. R., Webb, S. C., Saffer, D. M., et al. (2015). Downdip variations in seismic reflection character: Implications for fault structure and seismogenic behavior in the Alaska subduction zone. *Journal of Geophysical Research: Solid Earth*, *120*(11), 7883–7904. https://doi.org/10.1002/2015jb012338

Li, S., & Freymueller, J. T. (2018). Spatial variation of slip behavior beneath the Alaska peninsula along Alaska-aleutian subduction zone. *Geophysical Research Letters*, *45*(8), 3453–3460. https://doi.org/10.1002/2017gl076761

Li, Z., Wiens, D. A., Shen, W., & Shillington, D. J. (2024). Along-strike variations of Alaska subduction zone structure and hydration determined from amphibious seismic data. *Journal of Geophysical Research: Solid Earth*, *129*(3). https://doi.org/10.1029/2023jb027800

Lin, F., & Ritzwoller, M. H. (2011a). Helmholtz surface wave tomography for isotropic and azimuthally anisotropic structure. *Geophysical Journal International*, *186*(3), 1104–1120. https://doi.org/10.1111/j.1365-246x.2011.05070.x

Lin, F., & Ritzwoller, M. H. (2011b). Apparent anisotropy in inhomogeneous isotropic media. *Geophysical Journal International*, *186*(3), 1205–1219. https://doi.org/10.1111/j.1365-246x.2011.05100.x

Lin, F., Ritzwoller, M. H., & Snieder, R. (2009). Eikonal tomography: Surface wave tomography by phase front tracking across a regional broadband seismic array. *Geophysical Journal International*, *177*(3), 1091–1110. https://doi.org/10.1111/j.1365-246x.2009.04105.x

Lin, F., Ritzwoller, M. H., Yang, Y., Moschetti, M. P., & Fouch, M. J. (2011). Complex and variable crustal and uppermost mantle seismic anisotropy in the western United States. *Nature Geoscience*, *4*(1), 55–61. https://doi.org/10.1038/ngeo1036

Liu, C., & Ritzwoller, M. H. (2024). Seismic anisotropy and deep crustal deformation across Alaska. *Journal of Geophysical Research: Solid Earth*, *129*(5), e2023JB028525. https://doi.org/10.1029/2023JB028525

Liu, C., Sheehan, A., & Michael, R. (2024). Seismic azimuthal anisotropy model beneath the Alaska subduction zone (v0.1) [Dataset]. *Zenodo*. https://doi.org/10.5281/zenodo.10975884

Liu, C., Yao, H., Yang, H., Shen, W., Fang, H., Hu, S., & Qiao, L. (2019). Direct inversion for three-dimensional shear wave speed azimuthal anisotropy based on surface wave ray tracing: Methodology and application to yunnan, southwest China. *Journal of Geophysical Research: Solid Earth*, *124*(11), 11394–11413. https://doi.org/10.1029/2018jb016920

Liu, C., Zhang, S., Sheehan, A. F., & Ritzwoller, M. H. (2022a). Surface wave isotropic and azimuthally anisotropic dispersion across Alaska and the Alaska-aleutian subduction zone. *Journal of Geophysical Research: Solid Earth*, *127*(11). https://doi.org/10.1029/2022jb024885

Liu, C., Zhang, S., Sheehan, A. F., & Ritzwoller, M. H. (2022b). Surface wave isotropic and azimuthally anisotropic dispersion across Alaska and the Alaska-Aleutian subduction zone (Vol. *127*). [Dataset]. https://doi.org/10.5281/zenodo.7080282. *Zenodo* (11).

Lynner, C. (2021). Anisotropy-revealed change in hydration along the Alaska subduction zone. *Geology*, *49*(9), 1122–1125. https://doi.org/10.1130/g48860.1

Lynner, C., Toro-Acosta, C., Paulson, E., & Birkey, A. (2024). Local-S shear wave splitting along the length of the Alaska–Aleutian subduction zone. *Geophysical Journal International*, *237*(3), 1567–1574. https://doi.org/10.1093/gji/ggae107

Martin-Short, R., Allen, R., Bastow, I. D., Porritt, R. W., & Miller, M. S. (2018). Seismic imaging of the Alaska subduction zone: Implications for slab geometry and volcanism. *Geochemistry, Geophysics, Geosystems*, *19*(11), 4541–4560. https://doi.org/10.1029/2018gc007962

McPherson, A. M., Christensen, D. H., Abers, G. A., & Tape, C. (2020). Shear wave splitting and mantle flow beneath Alaska. *Journal of Geophysical Research: Solid Earth*, *125*(4). https://doi.org/10.1029/2019jb018329

Meyer, B., Saltus, B., & Chulliat, A. (2017). Version 3. *NOAA National Centers for Environmental Information*. [Dateset]. https://doi.org/10.7289/V5H70CVX. EMAG2v3: Earth magnetic anomaly grid (2-arc-minute resolution).

Miller, M. S., & Moresi, L. (2018). Mapping the alaskan moho. *Seismological Research Letters*, *89*(6), 2430–2436. https://doi.org/10.1785/0220180222

Montagner, J. P., & Nataf, H. C. (1986). A simple method for inverting the azimuthal anisotropy of surface waves. *Journal of Geophysical Research*, *91*(B1), 511–520. https://doi.org/10.1029/JB091iB01p00511

Müller, R. D., Sdrolias, M., Gaina, C., & Roest, W. R. (2008). Age, spreading rates, and spreading asymmetry of the world's ocean crust. *Geochemistry, Geophysics, Geosystems*, *9*(4). n/a-n/a. https://doi.org/10.1029/2007gc001743

Nayak, A., Eberhart-Phillips, D., Ruppert, N. A., Fang, H., Moore, M. M., Tape, C., et al. (2020). 3D seismic velocity models for Alaska from joint tomographic inversion of body-wave and surface-wave data. *Seismological Research Letters*, *91*(6), 3106–3119. https://doi.org/10.1785/0220200214

Richards, C., Tape, C., Abers, G. A., & Ross, Z. E. (2021). Anisotropy variations in the Alaska subduction zone based on shear-wave splitting from intraslab earthquakes. *Geochemistry, Geophysics, Geosystems*, *22*(5). https://doi.org/10.1029/2020gc009558

Schulte-Pelkum, V., Caine, J. S., Jones, J. V., & Becker, T. W. (2020). Imaging the tectonic grain of the northern cordillera orogen using transportable Array receiver functions. *Seismological Research Letters*, *91*(6), 3086–3105. https://doi.org/10.1785/0220200182

Seton, M., Müller, R. D., Zahirovic, S., Williams, S., Wright, N., Cannon, J., et al. (2020). A global dataset of present-day oceanic crustal age and seafloor spreading parameters. *Geochemistry, Geophysics, Geosystems*, *21*(10). https://doi.org/10.1029/2020GC009214

Shen, W., & Ritzwoller, M. H. (2016). Crustal and uppermost mantle structure beneath the United States. *Journal of Geophysical Research: Solid Earth*, *121*(6), 4306–4342. https://doi.org/10.1002/2016jb012887

Shillington, D. J., Bécel, A., Nedimović, M. R., Kuehn, H., Webb, S. C., Abers, G. A., et al. (2015). Link between plate fabric, hydration and subduction zone seismicity in Alaska. *Nature Geoscience*, *8*(12), 961–964. https://doi.org/10.1038/ngeo2586

Smith, M. L., & Dahlen, F. A. (1973). The azimuthal dependence of love and Rayleigh wave propagation in a slightly anisotropic medium. *Journal of Geophysical Research*, *78*(17), 3321–3333. https://doi.org/10.1029/JB078i017p03321

Tape, C., & Lomax, A. (2022). Aftershock regions of aleutian-Alaska megathrust earthquakes, 1938–2021. *Journal of Geophysical Research: Solid Earth*, *127*(7). https://doi.org/10.1029/2022jb024336

Uchida, N., Nakajima, J., Wang, K., Takagi, R., Yoshida, K., Nakayama, T., et al. (2020). Stagnant forearc mantle wedge inferred from mapping of shear-wave anisotropy using S-net seafloor seismometers. *Nature Communications*, *11*(1), 5676. https://doi.org/10.1038/s41467-020-19541-y

Venereau, C. M. A., Martin-Short, R., Bastow, I. D., Allen, R. M., & Kounoudis, R. (2019). The role of variable slab dip in driving mantle flow at the eastern edge of the alaskan subduction margin: Insights from shear-wave splitting. *Geochemistry, Geophysics, Geosystems*, *20*(5), 2433–2448. https://doi.org/10.1029/2018gc008170

Wang, F., Wei, S. S., Drooff, C., Elliott, J. L., Freymueller, J. T., Ruppert, N. A., & Zhang, H. (2024). Fluids control along-strike variations in the Alaska megathrust slip. *Earth and Planetary Science Letters*, *633*, 118655. https://doi.org/10.1016/j.epsl.2024.118655

Wang, X., Liu, X., Zhao, D., Liu, B., Qiao, Q., Zhao, L., & Wang, X. (2022). Oceanic plate subduction and continental extrusion in Sumatra: Insight from S-wave anisotropic tomography. *Earth and Planetary Science Letters*, *580*, 117388. https://doi.org/10.1016/j.epsl.2022.117388

Wang, Y., & Tape, C. (2014). Seismic velocity structure and anisotropy of the Alaska subduction zone based on surface wave tomography. *Journal of Geophysical Research: Solid Earth*, *119*(12), 8845–8865. https://doi.org/10.1002/2014jb011438

Wang, Z., Zhao, D., & Chen, X. (2022). Seismic anisotropy and intraslab hydrated faults beneath the NE Japan forearc. *Geophysical Research Letters*, *49*(2), e2021GL097266. https://doi.org/10.1029/2021GL097266

Wei, S. S., Ruprecht, P., Gable, S. L., Huggins, E. G., Ruppert, N., Gao, L., & Zhang, H. (2021). Along-strike variations in intermediate-depth seismicity and arc magmatism along the Alaska Peninsula. *Earth and Planetary Science Letters*, *563*, 116878. https://doi.org/10.1016/j.epsl.2021.116878

Xie, J., Ritzwoller, M. H., Shen, W., & Wang, W. (2017). Crustal anisotropy across eastern Tibet and Surroundings modeled as a depth-dependent tilted hexagonally symmetric medium. *Geophysical Journal International*, *ggx004*, ggx004. https://doi.org/10.1093/gji/ggx004

Yang, X., & Gao, H. (2020). Segmentation of the aleutian-Alaska subduction zone revealed by full-wave ambient noise tomography: Implications for the along-strike variation of volcanism. *Journal of Geophysical Research: Solid Earth*, *125*(11). https://doi.org/10.1029/2020jb019677

Yuan, K., & Beghein, C. (2018). A bayesian method to quantify azimuthal anisotropy model uncertainties: Application to global azimuthal anisotropy in the upper mantle and transition zone. *Geophysical Journal International*, *213*(1), 603–622. https://doi.org/10.1093/gji/ggy004

Zhang, S., Feng, L., & Ritzwoller, M. H. (2020). Three-station interferometry and tomography: Coda versus direct waves. *Geophysical Journal International*, *221*(1), 521–541. https://doi.org/10.1093/gji/ggaa046